Atmospheric Corrections Using MODTRAN for TOA and Surface BRDF Characteristics from High Resolution Spectroradiometric/ Angular Measurements from a Helicopter Platform

Yaping Zhou,① Ken C. Rutledge
Analytical Service & Material, Inc, Hampton, VA, USA
Thomas P. Charlock
Atmospheric Sciences Division, NASA Langley Research Center Hampton, VA, USA
Norman G. Loeb, Seiji Kato
Hampton University, Hampton, VA, USA

(Received September 1, 2000)

ABSTRACT

High-resolution spectral radiance measurements were taken by a spectral radiometer on board a helicopter over the US Oklahoma Southern Great Plain near the Atmospheric Radiation Measurements (ARM) site during August 1998. The radiometer has a spectral range from 350 nm to 2500 nm at 1 nm resolution. The measurements covered several grass and cropland scene types at multiple solar zenith angles. Detailed atmospheric corrections using the Moderate Resolution Transmittance (MODTRAN) radiation model and in-situ sounding and aerosol measurements have been applied to the helicopter measurements in order to retrieve the surface and top of atmosphere (TOA) Bidirectional Reflectance Distribution Function (BRDF) characteristics. The atmospheric corrections are most significant in the visible wavelengths and in the strong water vapor absorption wavelengths in the near infrared region. Adjusting the BRDF to TOA requires a larger correction in the visible channels since Rayleigh scattering contributes significantly to the TOA reflectance. The opposite corrections to the visible and near infrarred wavelengths can alter the radiance difference and ratio that many remote sensing techniques are based on, such as the normalized difference vegetation index (NDVI). The data show that surface BRDFs and spectral albedos are highly sensitive to the vegetation type and solar zenith angle while BRDF at TOA depends more on atmospheric conditions and the vi ewing geometry. Comparison with the Clouds and the Earth's Radiant Energy System (CERES) derived clear sky Angular Distribution Model (ADM) for crop and grass scene type shows a standard deviation of 0.08 in broadband anisotropic function at 25° solar zenith angle and 0.15 at 50° solar zenith angle, respectively.

Key words: BRDF, Radiative transfer, Atmospheric correction

1. Introduction

The classical definition of bi-directional reflectance-distribution function (BRDF) is a derivative, distribution function, relating the irradiance incident from one given direction to

①Corresponding author address: Dr. Yaping Zhou, Analysis Branch, Climate Prediction Center, NCEP/ NWS/ NOAA, WWB, 5200 Auth Road Camp Springs, MD 20746-4304.
Email: yzhou@ncep.noaa.gov

its contribution to the radiance reflected in another direction (Nicodemus et al., 1977)

$$f_r(\theta_i, \varphi_i; \theta_r, \varphi_r) = dL_r(\theta_i, \varphi_i; \theta_r, \varphi_r; E_i) / dE_i(\theta_i, \varphi_i) \qquad [sr^{-1}], \tag{1}$$

where θ (zenith angle) and φ (azimuth angle) together indicate a direction, the subscript i indicates quantities associated with incident radiant flux, the subscript r indicates reflected radiant flux, E_i is incident irradiance, L_r is reflected radiance, and d indicates a differential quantity.

In earth remote sensing, the angular distribution of the reflectance for incoming solar radiation at given solar zenith angle is crucial in converting radiances to the irradiance (Wielicki et al., 1996, Green and Hinton, 1996). The direction of the sun indicated by solar zenith angle (θ_0) and the direction for the reflectance (θ, φ) comprises the bidirectional concept in this context (where φ is relative to sun azimuth angle). The commonly used parameters describing BRDF characteristics include anisotropic parameter and bidirectional reflectance factor, etc. The anisotropic parameter is defined as the ratio of the equivalent Lambertion flux to the actual flux (Suttles et al., 1988). Let $M(\theta_0)$ be hemispheric reflected flux, $R(\theta_0,\theta,\varphi)$ for anisotropic function (ASF), then,

$$M(\theta_0) = \int_{\varphi=0}^{2\pi} d\varphi \int_{\theta=0}^{\pi/2} L(\theta_0,\theta,\varphi)\cos\theta\sin\theta d\theta, \tag{2}$$

$$R(\theta_0,\theta,\varphi) = \frac{\pi L(\theta_0,\theta,\varphi)}{M(\theta_0)}. \tag{3}$$

The ASF is widely used in the satellite Angular Distribution Model (ADM), which convert radiance measurements into fluxes. The ADM is normalized so that

$$\pi^{-1} \int_{\varphi=0}^{2\pi} d\varphi \int_{\theta=0}^{\pi/2} R(\theta_0,\theta,\varphi)\cos\theta\sin\theta d\theta = 1. \tag{4}$$

The BRDF reflectivity is defined as the ratio of actual radiance to the radiance from a perfectly diffuse nonabsorbing surface, following Capderou (1988)

$$\rho(\theta_0,\theta,\varphi) = \frac{\pi L(\theta_0,\theta,\varphi)}{E\cos\theta_0}. \tag{5}$$

This formula can be applied at the top of the atmosphere (TOA), where E is the TOA normal solar irradiance, that is, the solar constant corrected for the earth–sun distance. To bring down this formula to the surface, we can use the hemispherical downwelling flux (M_{dn}) instead of $E\cos(\theta_0)$ in (5), so that it becomes

$$\rho(\theta_0,\theta,\varphi) = \pi L(\theta_0,\theta,\varphi) M_{dn} \tag{6}$$

The surface BRDF, as defined above for this work, depends upon the sun, atmosphere, and viewing geometry, as well as the surface composition and structure. A more rigorously defined BRDF would be expressed as a function of two angles (incident and reflected) and be valid at particular wavelength (monochromatic); it would then indeed be a property of the surface and not depend uont the atmosphere or sun. We have adopted an alternative definition wherein the incident beam, which is enumerated by the solar zenity angle, also consists of diffuse radiation scattered downward by the atmosphere. Our BRDF span narrow wavelength intervals and are not monochromatic. The BRDFs of surface canopies are sometimes used for classifying the global ecosystem (Middleton, 1991; Li et al., 1996; Qin et al., 1998; Sanderm-

eier et al., 1999). Data collected in this study is mainly for (a) testing radiative transfer modeling and (b) improving satellite remote sensing of clouds and radiative fluxes.

Section 2 will introduce a helicopter BRDF campaign and the initial processing of the data. In Section 3, a radiative transfer model is used to correct the BRDF measurements to surface and TOA. Section 4 discusses the effect of atmospheric correction to the BRDF and the resulted surface and TOA BRDF characteristics. The last section summaries current work.

2. Data and initial processing

The CERES ARM Radiation Experiment (CARE) is a joint effort of the Clouds and the Earth's Radiant Energy System (CERES, Wielicki, B. A., et al., 1996) and the Atmospheric Radiation Measurement (ARM, Stokes and Schwartz, 1994). CERES is designed to provide comprehensive surface radiometric measurements and airborne scanning measurements of the bi-directional reflectance distribution function (BRDF) for a variety of ecosystems worldwide to validate and be incorporated into the CERES retrieval algorithm. The lack of agreement between thoery and measurement for shortwave in clear conditions in the CERES ARM GEWEX Experiment (CAGEX, Charlock and Alberta, 1996) and in the related sutdies (i.e., Kato et al., 1997) suggested the need for a better understanding of surface optics. The first CARE field campaign, CARE I, was conducted in north-central Oklahoma in the vicinity of the department of energy's Cloud and Atmospheric Radiation Testbed (CART) facility during August 1998. CERES has adopted the International Geo-sphere Biosphere Programme's (IGBP) surface characterization scheme in which the earth's surface is composed of 17 distinct homogeneous categories. The principal focus of CARE I was to provide comprehensive clear-sky BRDF measurements for mid-continental cropland during late summer. Coincident CERES Airborne Radiometer Scanner (ARS) reflected spectral directional radiance and upwelling irradiance measurements, CERES and CART site surface flux and aerosol measurements, and CERES / TRMM satellite observations constitute a comprehensive data set providing investigators with an opportunity to validate models and satellite retrieval algorithms.

North central Oklahoma in the vicinity of the SGP CART site is an agricultural region dominated by the production of winter wheat, and to a less degree, some soybeans, sorghum, grass, and alfalfa field. The predominant soil types in this area are either silt loam or silty clay loam in composition. Relief in this region is generally minor, less than 1 vertical meter relief per 500 horizontal meters. Pre-mission aerial and surface reconnaissance had selected five large homogeneous fields near the central facility for intensive BRDF study. The selected targets include fields of milo, soybean, alfalfa, grass and wheat (the wheat field was then fallow and consisted of bare soil, so it is referred to as bare soil in this paper). A typical CERES footprint in this region consists of a mosaic of such fields, each of which has a different spectral BRDF.

Airborne measurements were performed by the CERES ARS system. The system was carried aboard a Bell UH-1h helicopter. It was originally developed to derive desert BRDFs (Purgold et al., 1994) and later improved by adding GPS and other instruments (Wheeler et al., 1997). The system was updated for the CARE experiment to improve the data resolution and in-flight stability. A spectral radiometer with 5° field of view (FOV) was installed to provide the directional radiance measurements for the determination of BRDF estimates for a given surface target. Measurements were repeated for specific targets for multiple solar zenith angles from 75 degrees to 20 degrees. Each BRDF flight profile consists of a five-leg pattern

over a given target of interest (Fig. 1a shows the horizontal geometry). With respect to the sun azimuth angle, the legs were flown at 0, 20, 45, 90, and 135 degrees. During each leg of the pattern the target is "tracked" through a range of viewing zeniths from +75 degrees to −75 degrees. The vertical geometry of the maneuver is shown in Fig. 1b, wherein the helicopter flies from left to right. Measurements were taken from an altitude of 300 m Average Ground Level (AGL) at a nominal speed of 25.7 m/s. Data was collected at 4 Hz, corresponding to a resolution of approximately 1° in view zenity angle. As the instrument FOV (field of view) is 5°, the 300 m altitude results in average surface footprint diameters ranging from 27 m at nadir to approximately 408 m at 75° viewing zenith. It takes about 12 minutes for the helicopter to complete the 5−leg maneuver. The spectral resolution for the reflectance measurements is 1 nm over the range of 0.3 to 2.5 μm. These high viewing zenity angle and spectral resolution capabilities surpass those of some other existing systems (i.e., ASAS (Ranson et al., 1994); PARABOLA (Deering et al., 1992); and MODIS Airborne Simulator (MAS, King et al., 1996)) currently in use for BRDF validation studies.

A total of 31 complete BRDF measurements were obtained by the helicopter on six clear mornings during August 3−28, 1998. A "complete" BRDF means that the helicopter had completed all 5 legs (only 4 legs for milo at 25° solar zenith angle). Table 1 lists the julian days at which the BRDF measurements for a given scene (row) and approximate SZA (column) was taken. Note that the measurements for each scene type and SZA were generally not taken during the same day. Changes in local conditions during CARE I are not accounted in Table 1. For example: By tilting the stem of a plant, a gross change in wind speed (or direction when at high speed) can affect the BRDF as much as a change of a few degrees in SZA. Change in surface moisture due to precipitation or evaporation affects the albedo of exposed soil. Daily growth of the vegetation canopy also has an effect on BRDF.

Table 1. BRDF measurements taken during August 1998

SZA / Scene	25°	35°	40°	45°	50°	65°	70°	75°
Grass	229	219	219	219	219	219	219	219
Milo	229	X	228	227	227	226	226	226
Soybean	229	X	229	228	228	227	227	227
Bare Soil	229	X	227	218	226	218	218	218
Alfalfa	X	X	X	229	229	X	X	X

The raw data appear in different zenith angle intervals due to the combined effect of helicopter forward speed and pod angle rotation rates. Since the helicopter was pointing at the fixed surface target, the viewing zenith angle changes much faster near the nadir point than at the higher viewing zenith angles. The effective resolution for viewing zenith angle changes from about 0.2 degrees to 2.5 degrees and back to 0.2 degrees during one leg flight. Figure 2 shows the raw data of one BRDF measurement made at solar zenith angle of approximately 42° over the soybean field. Besides the noise which is likely related to the heterogeneity of the surface, peaks in the forward and backward directions are perceivable. The maximum radiance near the anti−solar direction (−42°) in Leg 1 is the signal of a hot spot (an increase in brightness at the viewing angle with minimum shadow).

The initial data processing includes converting the helicopter geometry into relative

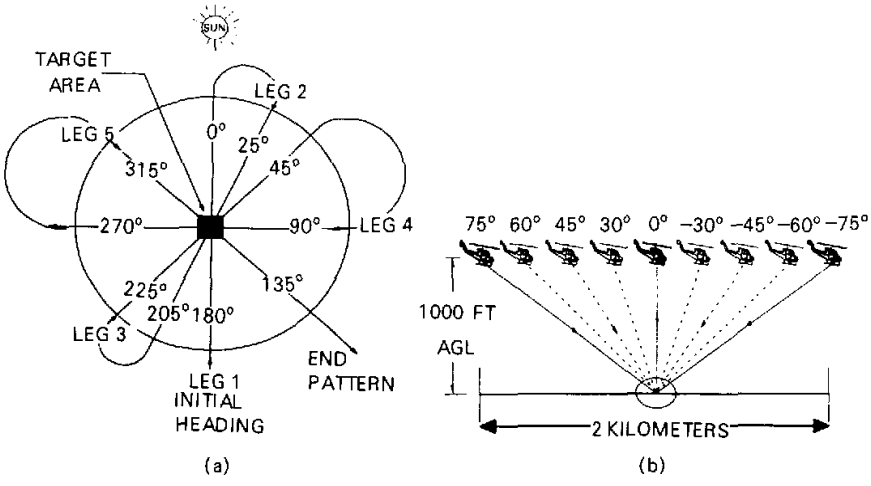

Fig. 1. CERES ARS flight profiles. (a) Horizontal view, (b) vertical leg profiles.

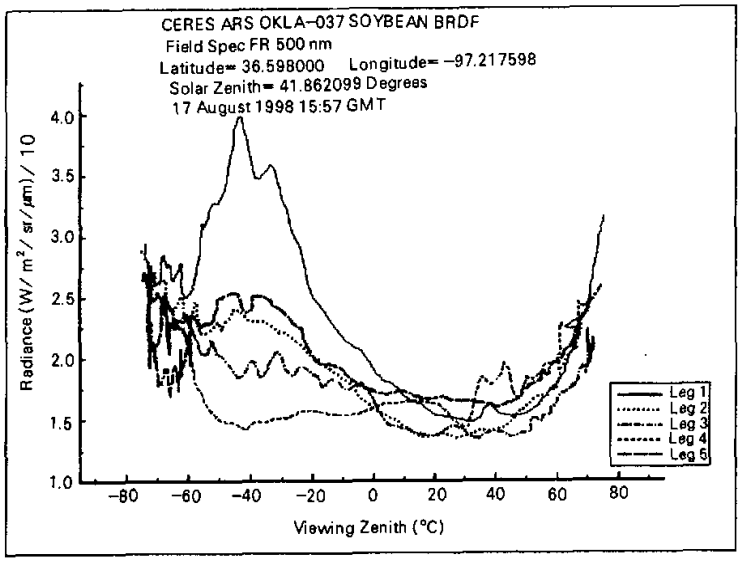

Fig. 2. The radiance measurements of 5 legs at one complete BRDF flight.

surface geometry, smoothing and re-sampling the radiance into regular 1° zenith angle grid. Data beyond the view zenith angle is of 70° are not used because they are usually noisy (partly due to large footprint size and difficulty of aiming at the ground target). A Lee filter (Lee, 1986) that smoothes additive noise by generating statistics in a local neighborhood was used

to minimize the measurement noise. Special attention was paid to the measurements near the hot spot area, where we avoided over smoothing by using a narrower window for the Lee filter.

The spectral albedos are calculated from spectral upwelling and downwelling fluxes. The downwelling flux was measured by a similar spectral radiometer with 180° FOV located near the surface in the central of the BRDF measurements. Upwelling flux was integrated from the helicopter radiance measurements using equation (2). The radiance beyond 70 degree viewing zenith angle was extrapolated; this will introduce some error. Interpolation in azimuth angle is also required, as the flight pattern (Fig. 1a) has only 5 legs. These high resolution spectral albedos in multiple solar zenith angles are a useful supplement of the BRDF measurements, they will be used to retrieve the surface and atmospheric radiation budget SARB in CERES and are suitable for application in GCM radiation packages.

3. Atmospheric correction

3.1 *A standard example*

To develop a BRDF for the surface with measurements taken by a helicopter, we must account for the intervening atmosphere; the change in radiant intensity through absorption and scattering by gases and aerosols in the path. While absorption and single scattering along the path tend to attenuate the radiance, multiple scattering into the path enhances the radiance. We have chosen a standard mid–latitude atmosphere with and without boundary layer aerosol to show the magnitude of the atmospheric correction for the visible and near infrared bands. This is most prominent between the helicopter level and TOA, and with the presence of aerosol. Figures 3a and 3b show that for visible band, the enhancement by multiple scattering is larger than the attenuation by absorption. The multiple scattering is even larger with the presence of boundary layer aerosols which also cause radiance peaks in the forward direction. For the near IR, due to gaseous absorption, the radiance at 300 m is weaker than at the surface. This is because both aerosol and molecular scattering optical depths decreases quickly with wavelengths while gaseous absorption mostly occurs in near IR. Figure 4 shows the radiance difference between TOA and surface. The correction patterns are similar to the previous figure with positive correction for visible band and negative correction for near IR in most angular region. The magnitudes of the correction for TOA are larger due to longer distance between the surface and TOA and hence larger optical depth in between. Under aerosol–loaded condition, both forward and backward directions have peak radiance at TOA due to the limb brightening effect of aerosol (forward) and rayleigh scattering (backward) in the visible band (Fig. 4b). For the near IR, the molecular scattering decreases more sharply than the scattering by particles so that in the backward direction, absorption dominates while in the forward direction, the aerosol forward scattering still dominates the absorption process (Fig. 4). The other important factor is that aerosol phase function is strongly forward peaked and molecular scattering phase function is symmetry in the forward and backward directions. The figures also show the angular dependence of the correction of radiance. The absorption is symmetric along azimuth direction with larger values occurring at higher viewing zenith angle where the absorption optical depth is larger (Figs. 3c and 4c). The multiple scattering of aerosol has peaks in the forward direction (Figs. 3b, 3d and Figs. 4b, 4d).

Thus atmospheric correction is needed to bring the helicopter BRDF measurements down to the surface. The same correction is required if these BRDF are to be used at the

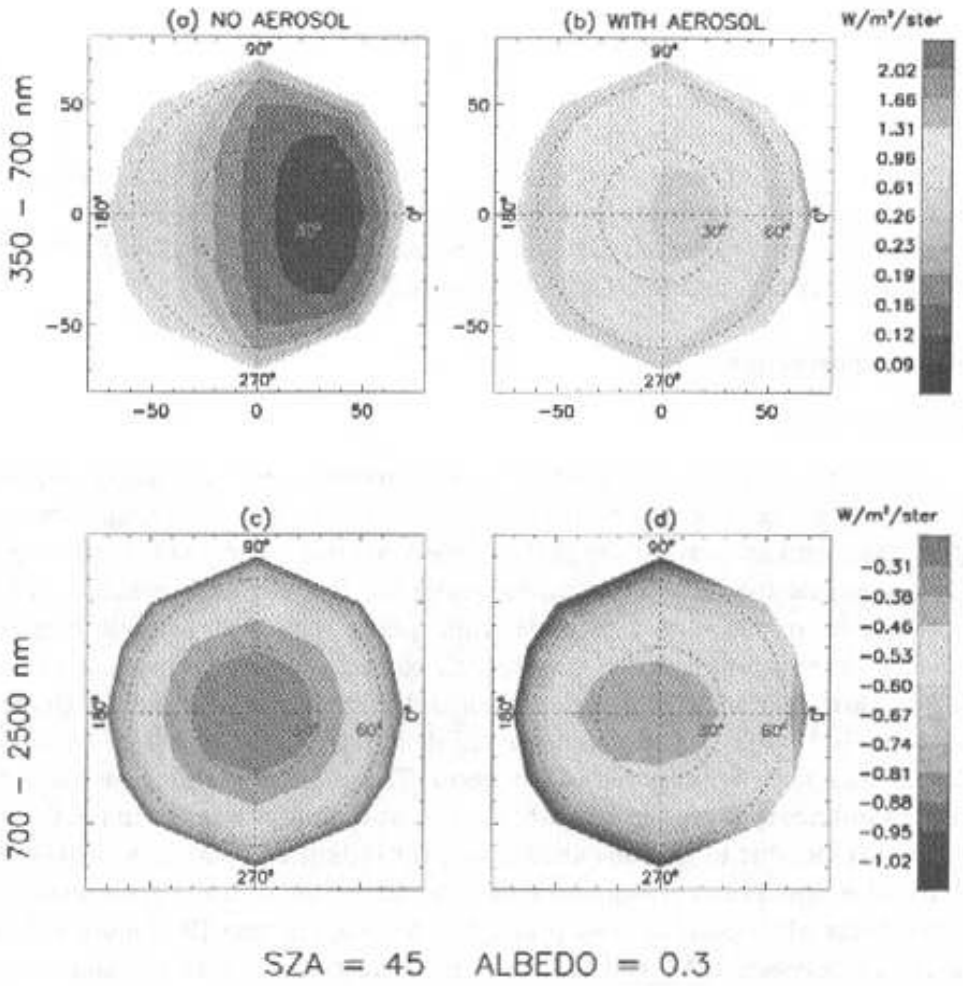

Fig. 3. MODTRAN computed radiance difference between 300 m and surface for a standard mid−latitude atmosphere. (a) Visible band (350−700 nm) without aerosol, (b) visible band with a boundary layer aerosol, (c) near IR band (700−2500 nm) without aerosol, (d) near IR band with a boundary layer aerosol.

TOA. There are many atmospheric correction algorithms, mostly for the correction from top of atmosphere to the surface or vise versa (Whitlock and Stuart, 1997; Wanner et al., 1997). In this study, we have employed a full radiative transfer model to conduct the required correction. The Moderate−Resolution Trnasmittance (MODTRAN) radiation model is chosen because it includes absorption, single scattering and multiple scattering processes involving both molecules and aerosols. It calculates atmospheric radiance and transmittance for wavenumbers from 0 to 50,000 cm^{-1} at a nominal spectral resolution of 2 cm^{-1} (Abreu and Anderson, 1996). The model fits the required spectral range and resolution with acceptable speed. It is used to compute the radiance difference at the helicopter and surface (or TOA) levels with in−situ soundings and aerosol profiles. The model calculated radiance difference tells how much correction is needed.

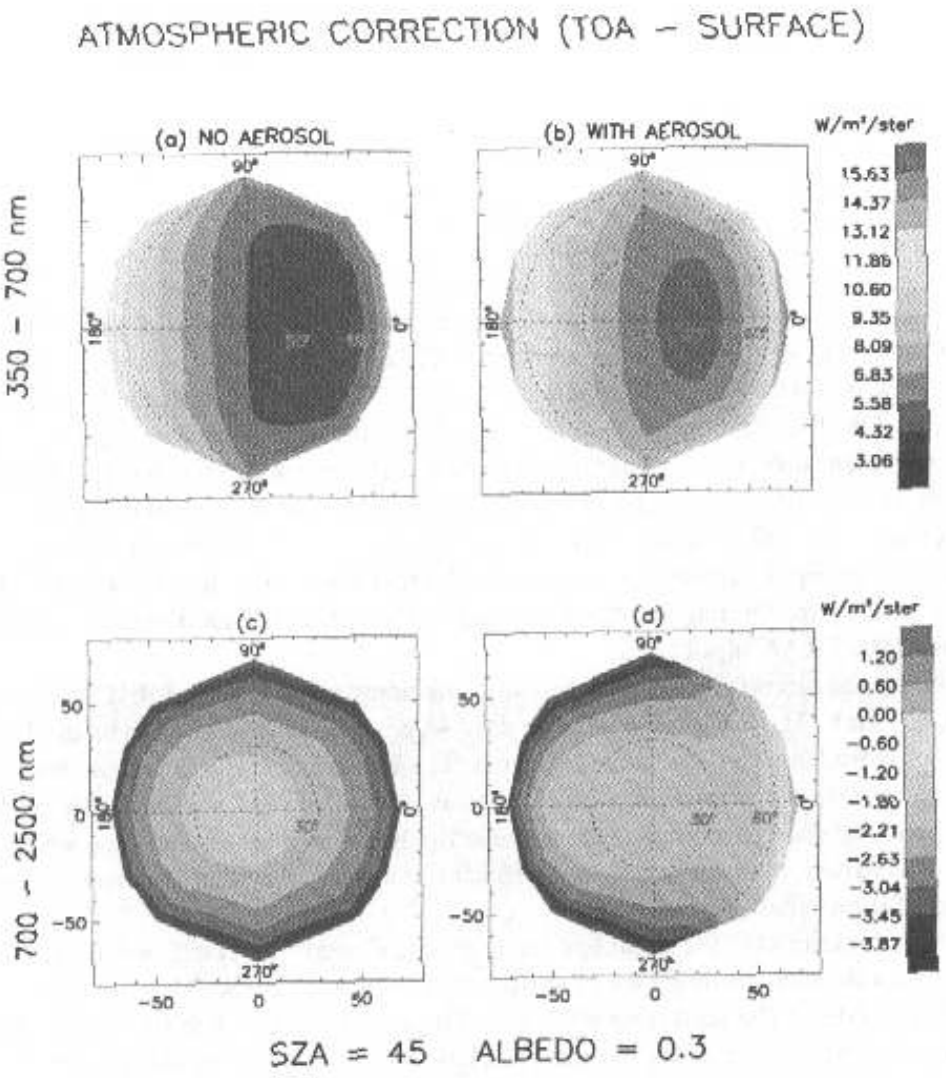

Fig. 4. The same as in Fig. 3, except for the radiance difference between TOA and surface.

3.2 *Input for BRDF correction*

The input to MODTRAN for the BRDF correction includes the atmospheric soundings which were launched before the helicopter took off. Since all the BRDF measurements were taken in the mornings, in case of clear days, a few completed BRDF measurements can be taken, such as on August 7 (see Table 1), and two or three soundings were launched in the same period of time. We averaged two or three sounding profiles for BRDF correction in order to simplify the processing and reduce the random errors in the sounding, based on the observation that the temperature and water vapor mixing ratio did not change dramatically in a short period of time. We use the sounding temperate, water vapor mixing ratio from surface to 12 km and the mid-latitude summer atmosphere above 12 km. The daily total ozone from TOMS (Total Ozone Mapping Spectrometer, http: // toms.gsfc.nasa.gov) is used to scale the default ozone profile and CO_2 mixing ratio is set as 355 ppmv.

As aerosol is important in the atmospheric correction while it is difficult to be measured accurately, we collected the aerosol measurements for the August 1998 period from different

instruments. Kato et al. (2000) have compared aerosol optical depth from airborne and ground–based measurements in ARM Oklahoma Central Facility for the period of August 1998. The airborne data were taken by a Gulf–stream aircraft from near surface to about 5 km over the central facility. The measurements include the scattering coefficient by an integrating nephelometer at wavelength of 450 nm, 550 nm and 700 nm and the absorption coefficient by a particle soot absorption photometer at wavelength 565 nm. The extinction coefficient at 550 nm is obtained by adding the scattering coefficient at 550 nm and absorption coefficient at 565 nm (assuming the absorption coefficint is the same for 565 nm and 550 nm). The aerosol optical depth derived from surface instrument include those from the multifilter rotating shadowband radiometer (MFRSR, Harrison et al., 1994) at wavelength of 415, 499, 620, 665, 862 nm and from Cimel sun–photometer operated by Aerosol Robotic Network (AERONET, Holben et al., 2000). Both instruments are estimated to have uncertainty of 0.01 for the optical depth. Since the total optical depth integrated from the extinction coefficient profile from aircraft does not match the optical depth derived from surface instrument, the MFRSR total aerosol optical depth at 550 nm is interpolated using Angstrom relation (Kato et al., 2000) and then used to scale the aircraft 550 nm extinction coefficient, which is used as input aerosol profile for the MODTRAN. The layer averaged absorption coefficient at 450 nm, 550 nm, 700 nm is normalized to extinction coefficient at 550 nm and also used as MODTRAN input.

However, the aircraft measurements only coincident with 3 days of BRDF measurements (Aug. 14, 15, and 17). For the other three days (Aug. 6, 7, and 16), we have used the extinction profiles from Raman Lidar measurements. The Raman Lidar uses aerosol backscattering property to retrieve the extinction coefficient at wavelength of 355 nm. MFRSR optical depth and Angstrom relations are used again to scale the Raman Lidar extinction coefficient to the 550 nm. Since there is no absorption coefficient available, we used the average absorption coefficient of the available three days.

The other parameter for complete description of aerosol optical property is the phase function which decides the direction of scattered radiation. The BRDF correction requires accurate information of the scattering direction. The aerosol size distribution and refractive index are basic parameters in order to estimate phase function using the Mie thoery. An alternative Henyey–Greenstein phase function uses only a single asymmetry parameter. The asymmetry parameter recorded for the average–continental aerosol ranges from 0.64 to 0.74 (d'Almeida et al., 1991). A median value of 0.68 which represents the asymmetry parameter at 80% relative humidity was chosen for this calculation.

The last important input for the model is the surface reflectivity. An ideal model for BRDF atmospheric correction should have a BRDF surface model as any radiation model should have, as the reflectance at surface can affect the amount the atmosphere modifies in the path. But MODTRAN3.7 has not yet incorporated surface BRDF capacity and even if it does, it would involve inversion process to input true surface BRDF. For the first order approximation, we would apply the observed spectral albedo which is available for each BRDF case from measurements (Fig. 5). They have captured detailed variation of albedo with the wavelength and solar zenith angle. True surface albedo can be derived using the corrected surface radiance, which means a few iterations will improve the results. For now, we consider that the direct spectral albedo as defined in the above are enough for the BRDF correction, we have to further resample the spectral albedo into 50 nm interval, since the model can only input limited number of spectral intervals.

4. Results and discussion

In order for the model to predict the atmospheric correction component, the basic requirement is for the model to be able to reproduce the observed radiance. Since MODTRAN only has a Lambertian surface, it is unlikely that model's radiance at 300 m should be the same as the helicopter measurements. The angular dependence of the observed radiance at 300 m is partly due to the anisotropic reflectance at the surface, and partly due to the atmospheric and aerosol effect. By taking out the atmospheric and aerosol effect, we can preserve the angular dependence of the surface. It is reasonable to require that the model be able to reproduce the observed downwelling flux since it does not depend on surface reflectivity as much so that it can be used to check that the input parameters are set up correctly.

Figure 6 shows surface downwelling fluxes and upwelling fluxes at 300 m from the model and observation for soybean field at solar zenith angle of 25°. From the figure, the model captures the spectral shape very well. It underestimates both the downwelling and upwelling flux around 700 nm to 1100 nm. The underestimate of upwelling can partly be contributed to the

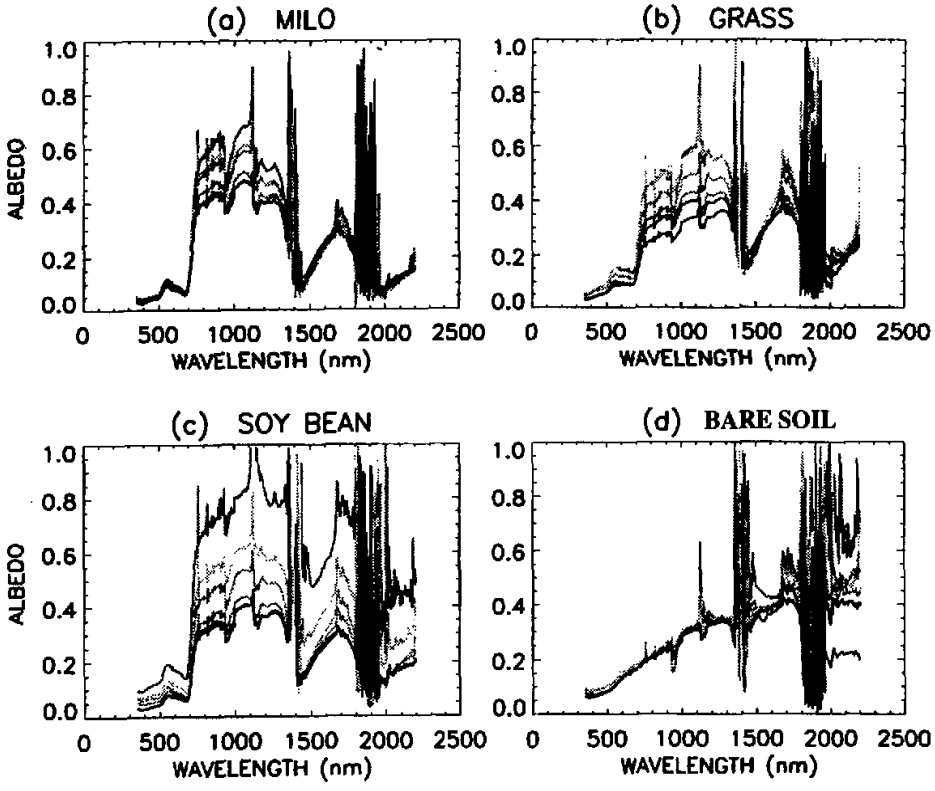

Fig. 5. Surface spectral albedos from measurements. Lines represent albedos at different solar zenith angle. (a) Spectral albedos for milo scene type, (b) for grass field, (c) for soybean field, (d) for bare soil.

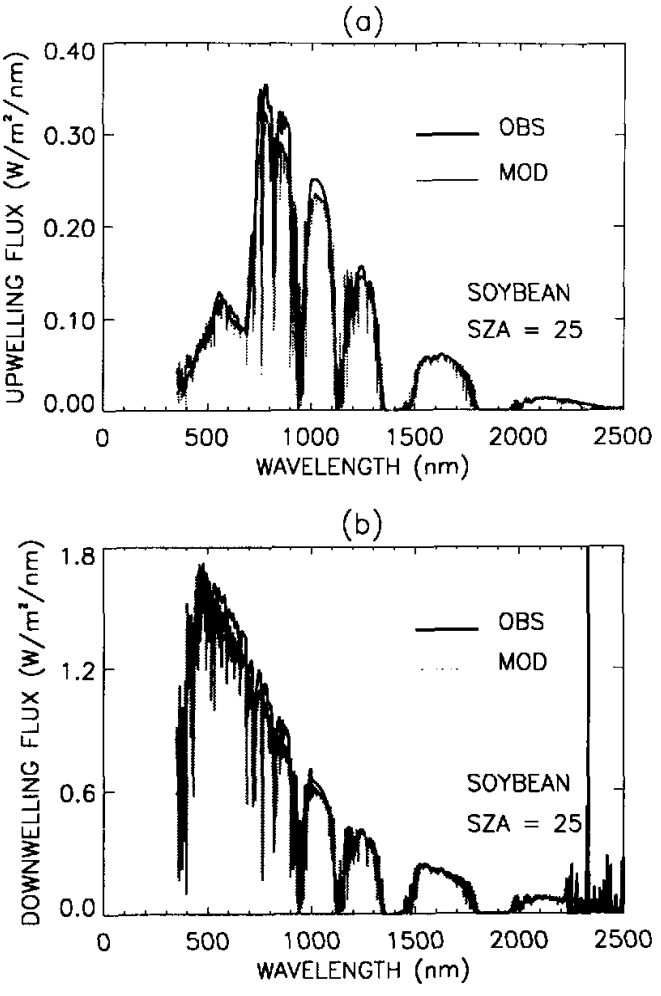

Fig. 6. MODTRAN computed upwelling flux and downwelling flux versus observed fluxes. (a) Upwelling fluxes at 300 m from model (light color) versus observed upwelling flux (dark color) for soybean field at solar zenith angle of 25°, (b) for downwelling fluxes at surface.

underestimate of downwelling flux. The other cases have similar result. Generally, the model's downwelling fluxes are within 10% of the observed surface downwelling fluxes and the upwelling fluxes are with 5%. The discrepancy between model and observations can come from many sources. Other than the model's assumptions, the input and the observed fluxes can be major sources of error. The spectral radiometer is carefully calibrated and the reported uncertainty is 5%. As the major difference occurs smoothly in the near infrared region, it is most likely related with aerosol specification. Since a thorough validation is not the task of this work, and what we want from the model is the radiance difference between the two levels,

this computation is considered adequate.

The actual atmospheric correction is quite consistent with what we saw from the standard case above. The difference of the spectral fluxes between 300 m and surface shows smooth positive values in visible regions and negative values in the near infrared (Fig. 7a). The former is mainly due to the dominating aerosol and molecular scattering over gas absorption. Both the molecular scattering (Rayleigh) and aerosol (Mie) scattering decrease with the

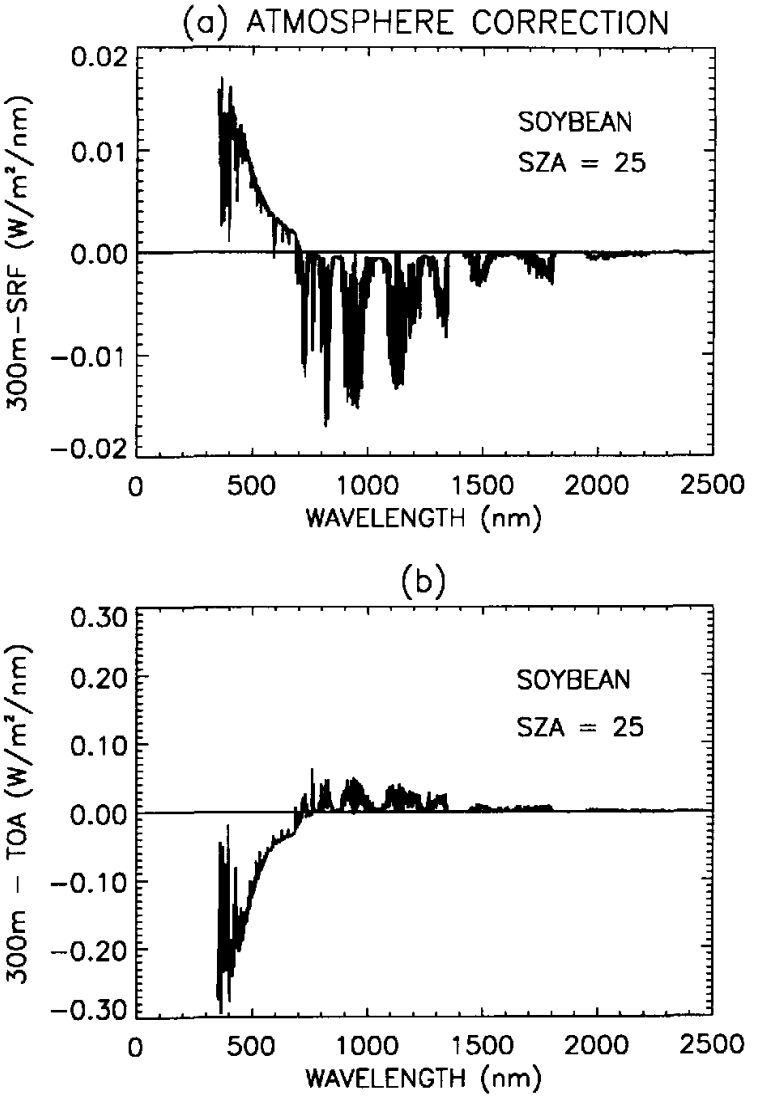

Fig. 7. Hemispheric integrated atmospheric correction with the wavelength. (a) For correction to the surface for soybean at 25° solar zenith angle, (b) for correction to the TOA at 25° solar zenith angle.

wavelength, especially for rayleigh scattering ($\tau \propto \lambda^{-4}$). In the near IR region, the major correction occurs in those strong absorption bands where line structures are obvious. The correction to TOA has the similar nature, but in the visible region, the TOA flux is far larger than the direct surface reflectance due to the back scattering and multiple scattering contributions of the whole atmospheric layer. The difference in the near IR is relatively small since most of the absorption occurs below 300 m and saturated line does not affect radiance from 300 m to TOA (Fig. 7b).

Figure 8 shows the anisotropic factor (ASF) of the soybean field at SZA of 25° at surface, helicopter level and TOA for wavelength 400 nm and 900 nm. Only BRDF at the helicopter level is direct measurement. The surface and TOA BRDF are corrected from the helicopter measurements. For the same scene type and same solar zenith angle, the surface BRDF shows strong hot spot in the anti–solar direction at 400 nm. At the TOA, hot spot is barely recognizable due to the overwhelming backscattering contributions. This is also shown in the albedo values. The albedo at the surface differs only slightly from the measurement due to the short distance, while the albedo at TOA is much larger. At 900 nm, the albedo at TOA is smaller than the surface albedo due to the absorption effect. The hot spot is still obvious.

Figure 9 shows the correction to spectral albedos for different scene types at 500 nm and 900 nm wavelengths with the change of solar zenith angle. At the visible channel, the albedo increases with the cosine SZA for all the scene types. The atmospheric correction not only makes the albedo value smaller but flatter with the solar zenith angle (Fig. 9a). The albedos in the visible channels are generally much smaller than the Near IR region due to the photosynthetic absorption by vegetation (Fig. 5). The relative correction at the near IR is smaller and depends on the absorption bands (Fig. 9b). The opposite change of radiance at visible wavelengths and near IR wavelengths will affect the radiance difference or ratio which many remote sensing techniques are based on. For example, the normalized difference vegetation index (NDVI) is computed from the radiance at one visible channel and one near IR channel (Pinker and Laszlo, 1992). In Fig. 10, NDVI computed from nadir radiance at 500 nm and 900 nm are shown for three scene types at TOA, 300 m and surface. For soybean and grass fields, NDVI at 300 m is around 0.4 and 0.3 respectively. NDVI at surface is systematically larger than the ones at 300 m (Figs. 10a and 10b). The NDVI at TOA is negative since radiance at 500 nm is larger than at 900 nm at TOA due to back scattering contribution to visible channel and absorption in the near IR. The NDVI for bare soil is very small at surface due to little vegetation (Fig. 10c).

The grass field ASF at selected wavelengths (500 nm and 900 nm) and solar zenith angles (25° and 65°) are shown in Fig. 11. The variation of surface BRDF with the wavelength and solar zenith angle is well represented here. The hot spot signal is most prominent at 500 nm at the solar zenith angle of 25° (Fig. 11a). The same plot shows that for visible channel, the overall reflectance at backward direction is stronger than the forward direction. At 900 nm, the surface is less anisotropic as the ASF has small variation (note that a Lambertian surface will have uniform ASF of unit). At high solar zenith angle (65°), both forward and backward scattering peaks are prominent at 500 nm (Fig. 11c) while the peak shifts toward more backward at 900 nm (Fig. 11d).

The BRDF at TOA has similar pattern and variations as at the surface (Fig. 12). The hot spot signal is less obvious at 500 nm even at small solar zenith angle (Fig. 12a). The forward and backward scattering at high viewing zenith angle (the limb brightening) is much stronger at high solar zenith angle (Figs.12c and 12d). It demonstrates the necessity to carefully treat

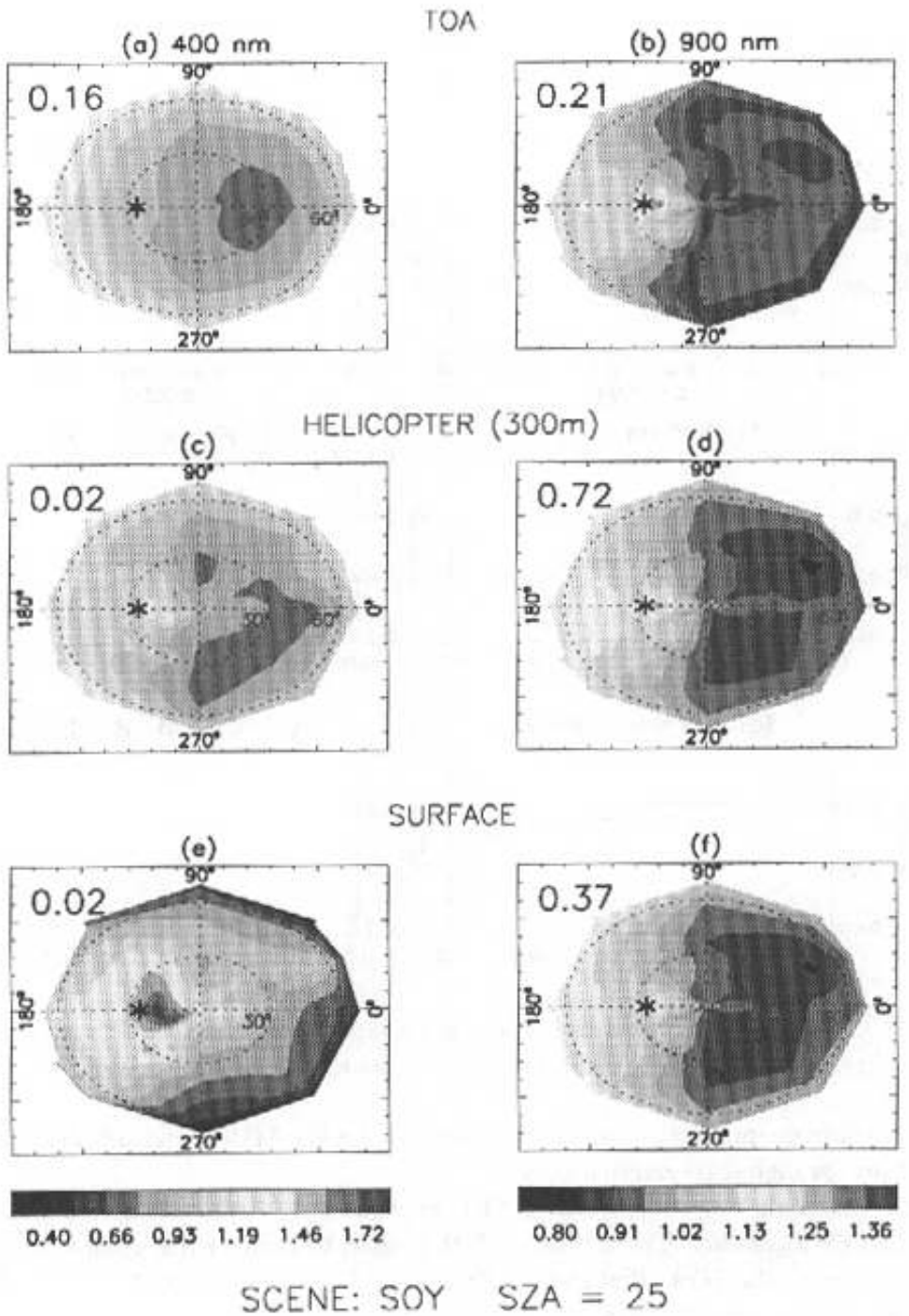

Fig. 8. Anisotropy factor derived at TOA, helicopter level and surface for 400 nm and 900 nm channels for soybean at 25°. The numbers at the up right corner are the albedo for that wavelength.

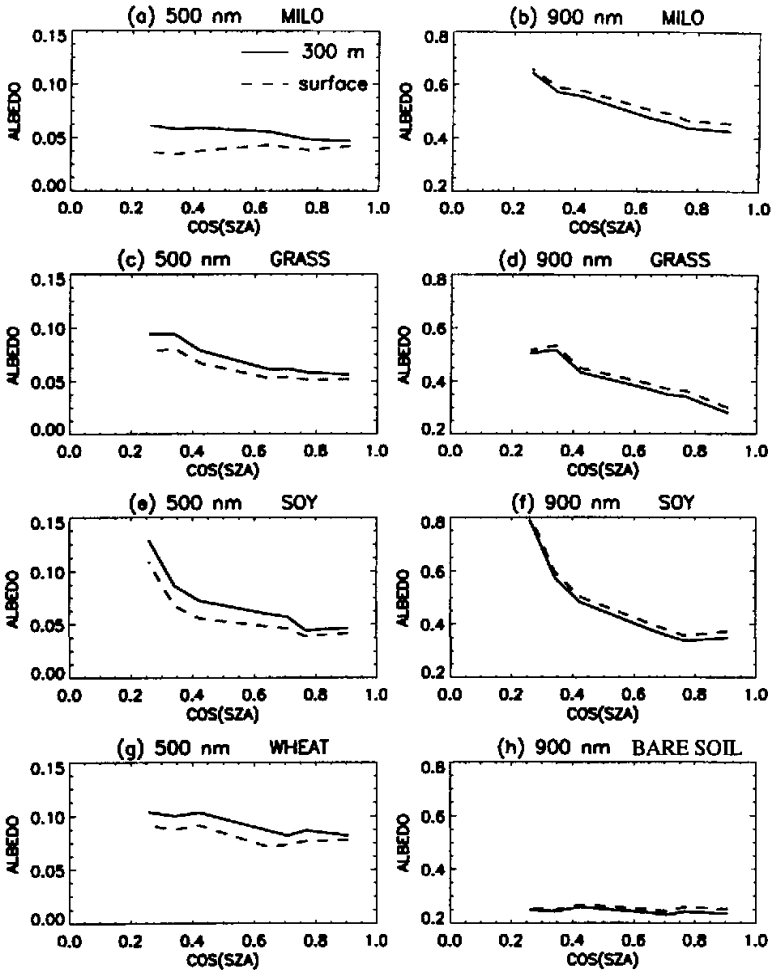

Fig. 9. Spectral albedos with the cosine of solar zenith angle at surface and 300 m. The left panels are for wavelength at 500 nm, the right panels for wavelength at 900 nm.

the TOA anisotropy properties such as required by CERES ADM (angular dependence model), especially for high solar zenith angles.

One of the main objectives of the CARE experiment is to provide a validation data set for the CERES algorithm. The CERES ADM is used to convert the satellite measured radiance to fluxes at the TOA. Preliminary clear sky ADMs from CERES TRMM have been constructed based on 80 days of CERES Rotating Azimuth Plane (RAP) scanner measurements. It follows the IGBP classification of ground scene type. The BRDF brought up to the TOA in this study should be directly comparable to the CERES clear sky ADM for the same scene types, although the former is based on a particular location and a particular day, while the later is a blend of measurements for the scene type at different times.

Figure 13 compares the ASF of different scenes at solar principle plane at selected solar

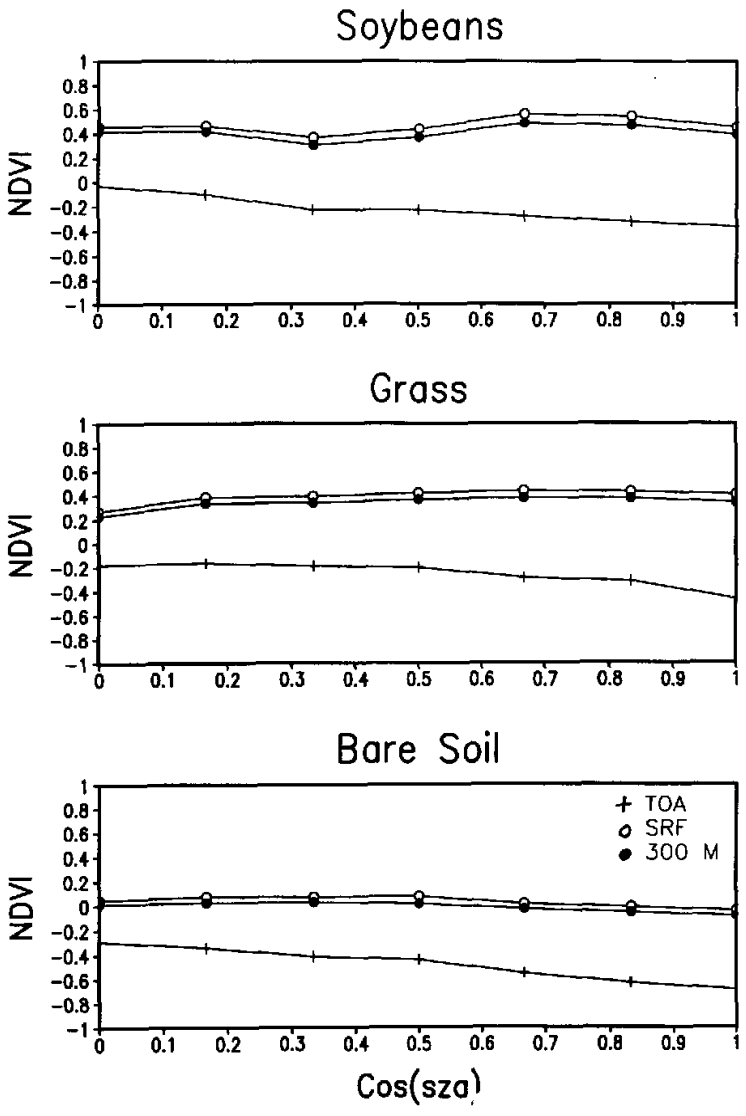

Fig. 10. NDVI at surface, 300 m and TOA with the cosine of solar zenith angle for soybean, grass and bare soil field.

zenith angle (25° and 50°).The 500 nm ASF of the four scenes at surface differ quite obviously at both 25° and 50° solar zenith angle due to different vegetation structure (Figs. 13a and 13b). The milo and grass field have the largest contrast in the forward and backward direction. The bare soil has the smallest variation along the principle plane. The intensities of hot spots for difference scenes are quite different. The BRDF at the same wavelength at TOA has less variation for different scene types as the atmospheric effect has smoothed out the surface difference (Figs. 13c and 13d). The hot spot at 25° solar zenith angle is much weaker but

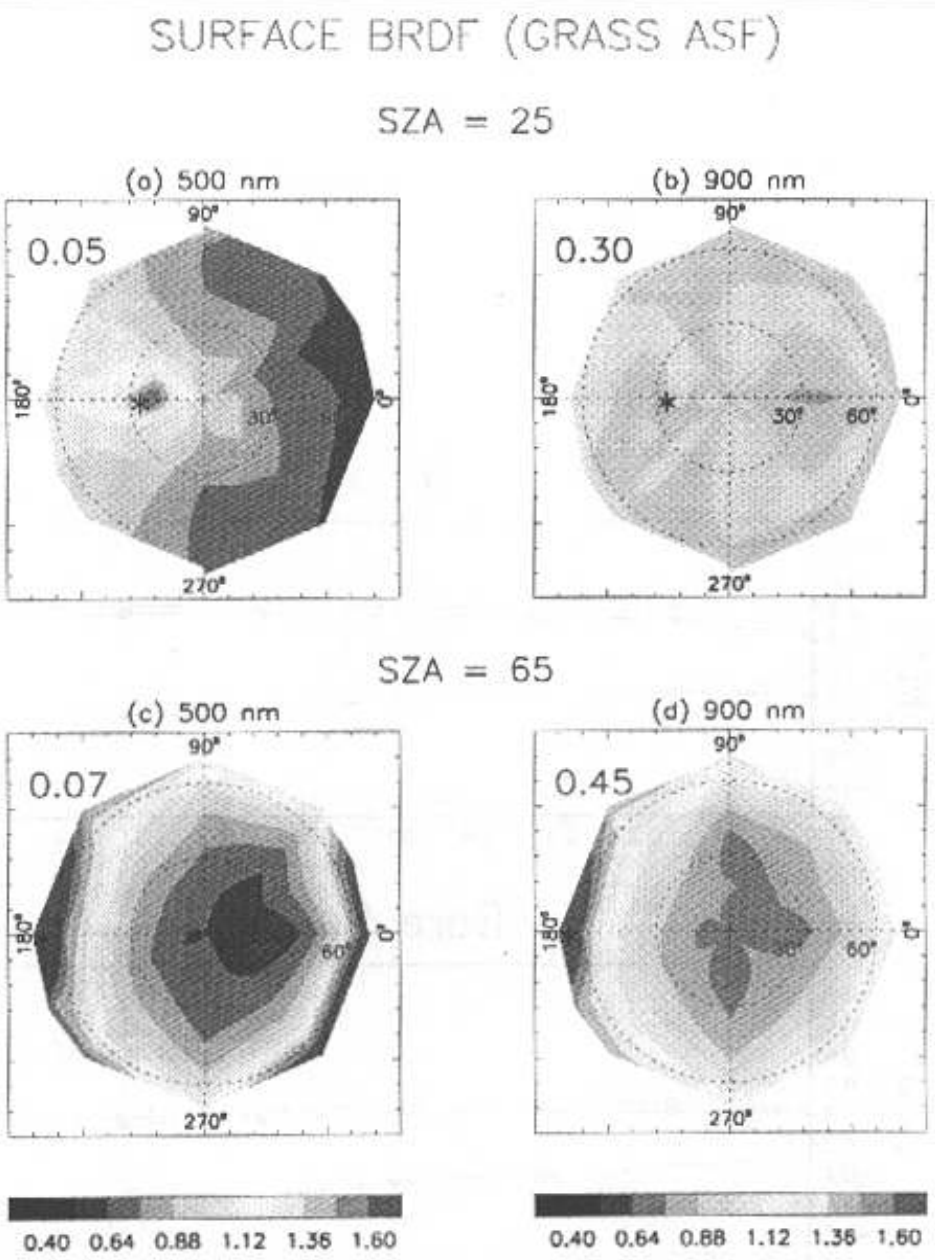

Fig. 11. Surface BRDF (ASF) for grass field at (a) 500 nm and solar zenith angle of 25°, (b) 900 nm and solar zenith angle of 25°, (c) 500 nm and solar zenith angle of 65°, (d) 900 nm and solar zenith angle of 65°.

still visible (Fig. 13c). Figures 13e and 13f show the broadband BRDF from CARE (integrated from 350 nm to 2200 nm) as well as CERES ADMs for the cropland and grass. We can see that the CERES ADMs match the corrected BRDF quite well. The large difference occurs at high viewing zenith angle at 50° solar zenith angle. The CERES ADM has larger ASF than CARE at backward direction while smaller in the forward direction. Besides that the data are collected at different time (thus different atmospheric and aerosol conditions), the CARE BRDF at TOA may have over corrected at forward direction and under corrected at the backward direction because of the Lambertian surface assumption. The peak near 50° view zenith angle in the forward direction for CERES crop is likely observational error.

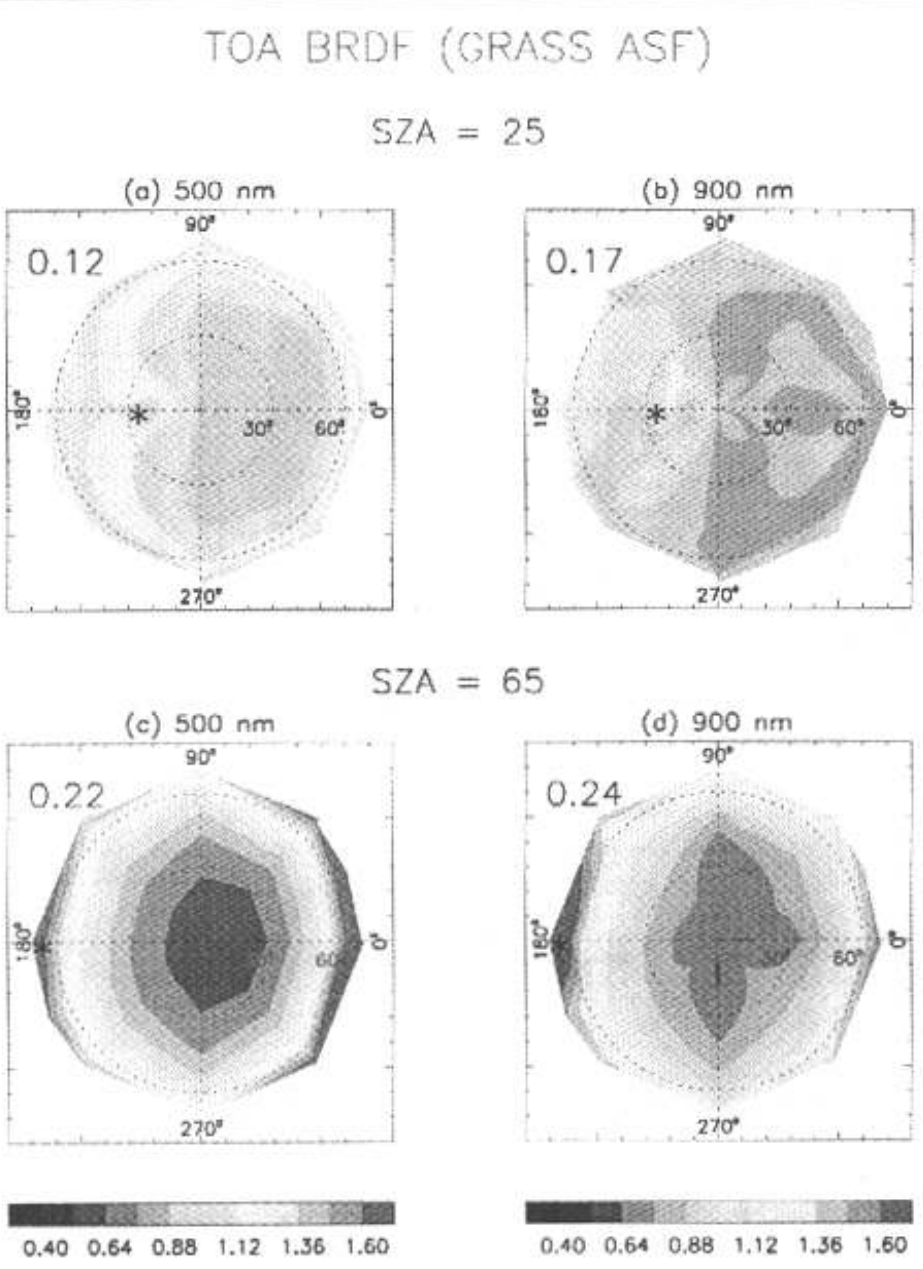

Fig. 12. Same as Fig. 1 except at TOA.

The rms of ASF between CARE cropland (milo and soybean) and CERES crop / mosaic is 0.07 at 25° solar zenith angle and 0.13 at 50° solar zenith angle. For the grass field, the rms are 0.08 and 0.15 at 25° and 50° solar zenith angle, respectively.

5. Concluding remarks

A total of 31 BRDF measurements were taken during CERES ARM Radiation Experiments (CARE I) by the ARS helicopter platform during August 1998. These measurements utilize multiple sensors to obtain helicopter directional spectral radiance measurements and ground hemispheric flux estimates. The helicopter BRDF measurements are corrected to surface as well as top of atmosphere using MODTRAN radiation model and in-situ atmospher-

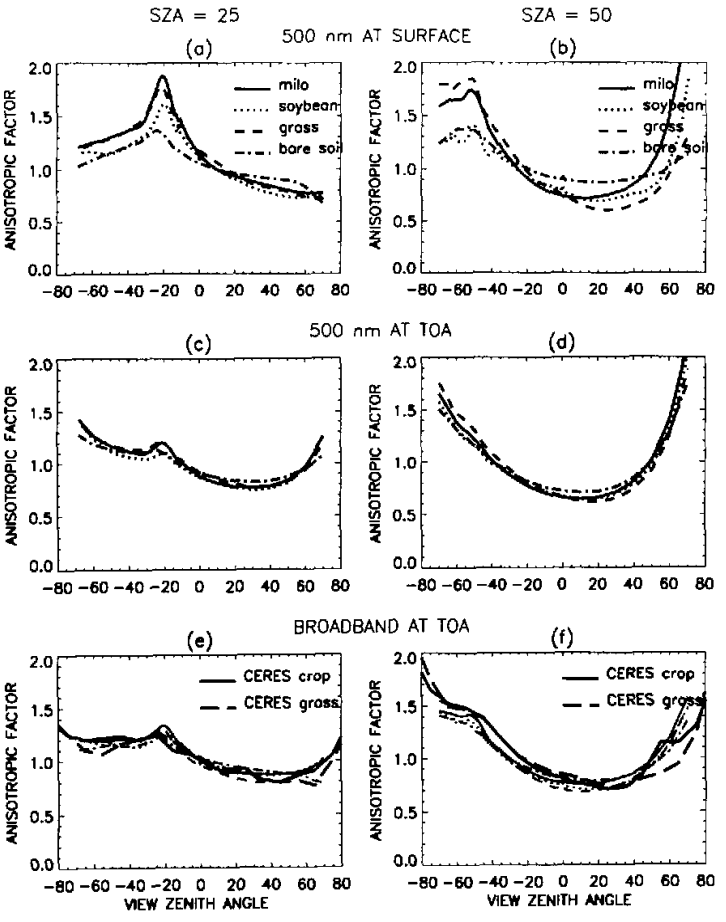

Fig. 13. Anisotropic factors at principle plane for (a) milo (solid line), soybean (dotted line), grass (dashed line) and bare soil (dash dotted line) field at 500 nm and solar zenith angle of 25° at surface, (b) same as (a) except at solar zenith angle of 50°, (c) same as (a) except at TOA, (d) same as (a) except at solar zenith angle of 65° and TOA, (e) CERES broadband ASF at principle plane for crop / mosaic (dark solid line), grass (dark dashed line) field versus CARE derived broadband ASF for milo, soybean, grass and bare soil fields at solar zenith angle of 25°, (f) same as (e) but at solar zenith angle of 50°.

ic soundings and aerosol measurements.

The atmospheric correction to surface results in weaker radiance at visible wavelengths and stronger radiance at near infrared absorption bands. The correction to TOA is much larger and has opposite effect. The opposite change in visible and near IR can affect spectral difference or ratio which many remote sensing techniques are based on, such as the normalized differential vegetation index (NDVI).

From these measurements, it is found that surface BRDF is very sensitive to the scene type as well as the viewing geometry. The BRDF at TOA is less sensitive to subtle variation of

surface scene type but depend more on atmosphere and aerosol conditions. Considerable agreement is found when comparing the BRDF corrected to TOA from this work with the CERES clear sky ADM for vegetation and grass fields. Large discrepancy is likely to appear at high solar zenith angle and high viewing zenith angle, in which case the atmosphere and aerosol multiple scattering play an important role.

We have been benefited significantly from discussions with Dr. Y. Hu, C. Whitlock and F. Rose in the course of this work. D. Rutan provided the MFRSR data for August 1998. This work is supported by NASA NASI-19570.

REFERENCES

Abreu, L.W., and G. P. Anderson, 1996: The MODTRAN 2 / 3 Report and LOWTRAN 7 Model, prepared by Ontar Corporation for PL / GPOS.

Capderou, M., 1998: Determination of the Shortwave Anisotropic Function for Clear-Sky Desert Scenes from ScaRaB Data: Comparison with Models Issued from Other Satellite Data, *J. Appl. Meteor.*, **37**, 1398–1411.

Charlock, T.P., and T.L. Albeta, 1996: The CERES / ARM / GEWEX experiment (CAGEX) for the retrieval of radiative fluxes with satellite data. *Bull. Am. Meterol. Soc.*, 77, 2673–2683.

d'Almeida, G. A., P. Koepke, and E. P. Shettle, 1991: *Atmospheric aerosols – global climatology and radiative characteristics*. A. Deepak Publishing, Hampton, Virginia, 561 pp.

Deering, D. W., E. M. Middleton, J. R. Irons, B. L. Blad, E. A. Walter-Shea, C. J. Hays, C. Walthall, T. F. Eck, S. P. Ahmad, and B. P. Banerjee, 1992: Prairie grassland bidirectional reflectances measured by different instruments at the FIFE site. *J. Geophys. Res.*, **97**, 18887–18903.

Green, R. N., and P. O. Hinton, 1996: Estimation of angular distribution models from radiance pairs. *J. Geophys. Res.*, **101**, 16951–16959.

Holben, B. N., D. Tanre, A. Smirnov, T. F. Eck, I. Slutsker, N. Abuhassan, W. W. Newcomb, J. Schafer, B. Chatenet, F. Lavenue, Y. J. Kaufman, J. Vande Castle, A. Setzer, B. Markham, D. Clark, R. Frouin, R. Halthore, A. Karnieli, N. T. O'Neill, C. Pietras, R. T. Pinker, K. Voss, G. Zibordi, 2000: An emerging ground based aerosol climatology: Aerosol Optical Depth from AERONET, submitted to *J. Geophys. Res.*.

Kato, S., T.P. Ackerman, E.E. Clothiaux, J.H. Mather, G.G. Mace, M.L. Wesely, F. Murcray, and J. Michalsky, 1997: Uncertainties in modeled and measured clear-sky surface shortwave irradiances. *J. Geophys. Res.*, **102**, 25,881–25,898.

Kato, S., M. H. Bergin, T. P. Ackerman, T. P. Charlock, E. E. Clothiaux, R. A. Ferrare, R. N. Halthore, N. Laulainen, G. G. Mace, J. Michalsky, and D. D. Turner, 2000: A comparison of the aerosol thickness derived from ground-based and airborne measurements. *J. Geophy. Res.*, **105**, 14701–14717.

Lee, 1986: Speckle suppression and analysis for synthetic aperture radar images. *Optical Engineering*. **25(5)**, 636–646.

Li, Z., J. Cihlar, X. Zheng, L. Moreau, and H. Ly, 1996: The bidirectional effects of AVHRR measurements over boreal regions. *IEEE Trans. Geosci. Remote Sens.*, **34**, 1308–1322.

Middleton, E. M., 1991: Solar zenith angle effects on vegetation indices in tallgrass prairie, *Remote Sens. Environ.*, **38**, 45–62.

Nicodemus, J.C. Richmond, J.J. Hsia, I.W. Ginsberg, and T. Limperis, 1997: *Geometrical Considerations and Nomenclature for Reflectance*. NBS Monograph 160.

Pinker, R. T., and I. Laszlo, 1992: Global distribution of photosynthetically active radiation as observed from satellites. *J. Climate*, **5**, 56–65.

Purgold, G. C., C. H. Whitlock, R. J. Wheeler, and S. R. LeCroy, 1994: A multiwavelength airborne radiometer scanner (ARS) for measuring surface bi-directional reflectance characteristics. *Remote Sens. Environ.*, **47**, 322–330.

Qin, W., S. Gerstl, and D. W. Deering, 1998: Examination of relations between NDVI and vegetation properties using simulated MISR data. *Proceedings of IGARSS'98*, IEEE, Seattle, Washington. 1243–1245.

Ranson, K. J., J. R. Irons, and D. L. Williams, 1994: Multispectral Bidirectional Reflectance of Northern Forest Canopies with the Advanced Solid-State Array Spectroradiometers (ASAS). *Remote Sens. Environ.*, **47**,

276–289.

Sandmeier, S. R., E. M. Middleton, D. W. Deering, and W. Qin, 1999: The potential of hyperspectral bidirectional reflectance distribution function data for grass canopy characterization. *J. Geophy. Res.*, **104**, 9547–9560.

Stokes, G. M., and S. Schwartz, 1994: The atmospheric radiation measurement (ARM) program: programmatic background and design of the cloud and radiation test bed. *Bull. Amer. Meteor. Soc.*, **75**, 1201–1221.

Suttles, J. T., R. N. Green, P. Minnis, G.L.Smith, W.F. Stayor, B. A. Wielicki, I.J.Walker, D. F. Young, V. R. Taylor, and L. L. Stowe, 1988: *Angular Radiation Models for Earth–Atmosphere System, in short wave radiation*, Vol. 1, NASA reference Publication 1184, 144pp.

Wanner, W., A. Strahler, B. Hu, P., Lewis, J.P. Muller, J. P., X. Li, Barker Schaaf, C., and Barnsley, M., 1997: Global retrieval of BRDF and albedo over land from EOS MODIS and MISR data: Theory and algorithm. *J. Geophys. Res.*, **102**, 17143–17162.

Wheeler, R. J., G. C. Purgold, and C. H. Whitlock, 1997: The CERES airborne radiometerscanner. *Ninth conference on Atmospheric Radiation*. Long Beach, California, February 2–7.

Whitlock, C. H., and S. R. LeCroy, 1997: Theoretical / experimental validation of CERES / ERBE TOA SW angular distribution models. *AMS Ninth Conference on Atmospheric Radiation*. Long Beach, California, February 2–7.

Wielicki, B. A., and B. R. Barkstrom, E. F. Harrison, R. B. Lee III, G. L. Smith, and J. E. Cooper, 1996: Cloud and the Earth's Radiance Energy System (CERES): An earth observing system experiment. *Bull. Amer. Metero. Soc.*, **77**, 853–868.